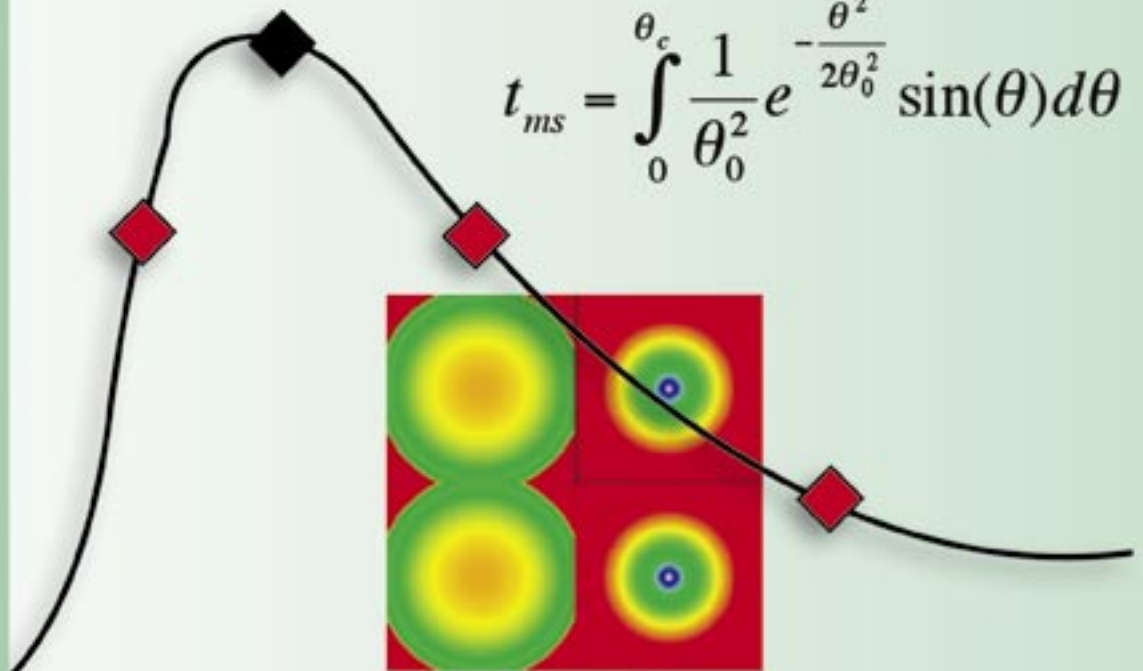
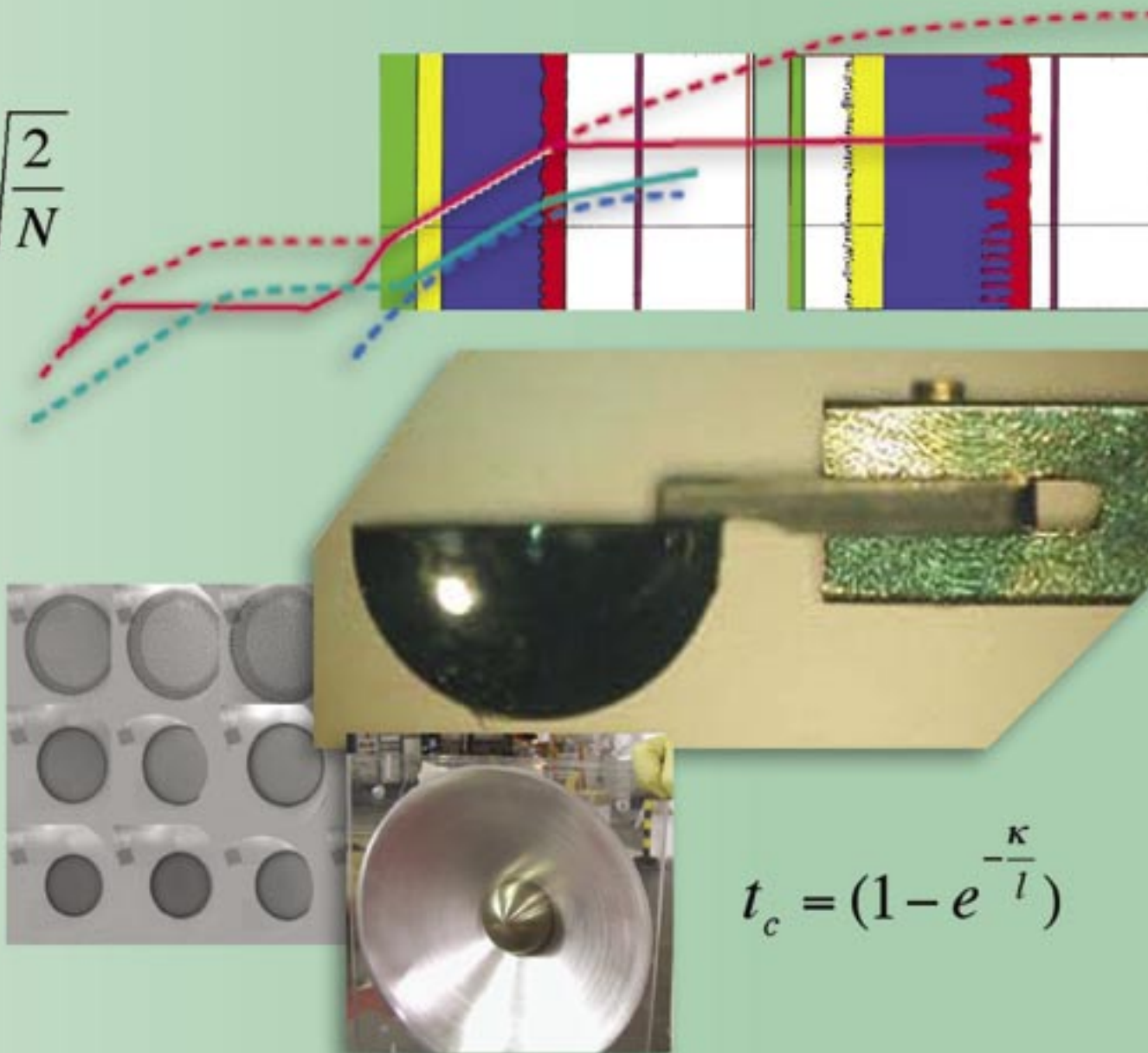


$$t_{ms} = \int_0^{\theta_c} \frac{1}{\theta_0^2} e^{-\frac{\theta^2}{2\theta_0^2}} \sin(\theta) d\theta$$



Facilities

$$\frac{\Delta L}{L} = \sqrt{\frac{2}{N}}$$



$$t_c = (1 - e^{-\frac{\kappa}{l}})$$

Facilities Contents

Research Highlights

Trident Laser Laboratory	201
Charged-Particle Radiography—Providing New Methods of Imaging	205
Shock-Wave and Material-Properties Experiments Using the Atlas Pulsed-Power Machine	209

Project Descriptions

Relocation of Atlas to the Nevada Test Site	213
High-Energy Ultra-Short Laser Pulses at Trident	214
Trident Laboratory Operations	215

Trident Laser Laboratory

Lasers—light amplification by stimulated emission of radiation—are among the most varied and versatile tools of modern science and technology. LANL has been a leader in laser technology since the early 1970s, particularly in the arena of high-energy pulsed lasers. The latest of these is Trident, a multipurpose laboratory that principally supports ICF, HED physics, and basic research. Since becoming operational in 1993, Trident has fired over 800 high-energy target shots (Figure 1) each year for experiments requiring high-energy pulsed laser light.

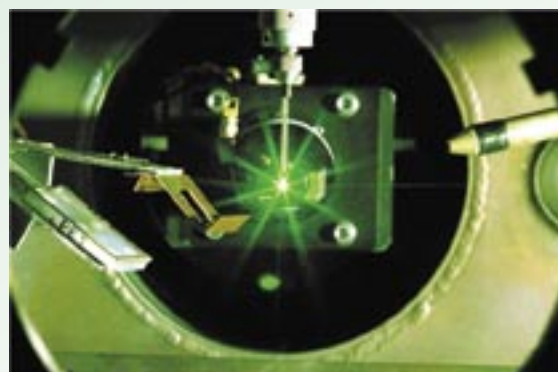
*F.L. Archuleta, R.B. Gibson,
R.P. Gonzales, T.R. Hurry,
R.P. Johnson, N.K. Okamoto,
T.A. Ortiz, T. Shimada (P-24)*

The Trident laser laboratory provides varied and flexible experimental configurations for a wide variety of experiments. It features a powerful Nd:glass laser driver with flexible characteristics in pulse shape, duration, intensity, and focus; two well-instrumented vacuum target chambers with a suite of resident optical and x-ray diagnostics; and ancillary equipment and facilities for optical fabrication and diagnostic checkout. A dedicated staff maintains and operates the Trident laboratory and assists users. The Target Fabrication Facility in the MST Division at LANL designs, fabricates, and characterizes targets for experiments conducted on Trident. Users from more than a dozen major research institutions have executed ~ 200 experimental campaigns in the past decade, including studies of x-ray generation and diffraction, plasma waves and instabilities, shock waves in solids and gases, energetic proton and ion generation, and EOS and other material properties. In addition, high-speed plasma and x-ray diagnostic techniques and instruments are routinely developed and tested at the laboratory for use on Trident and at other major laser laboratories.

Trident Laser Driver

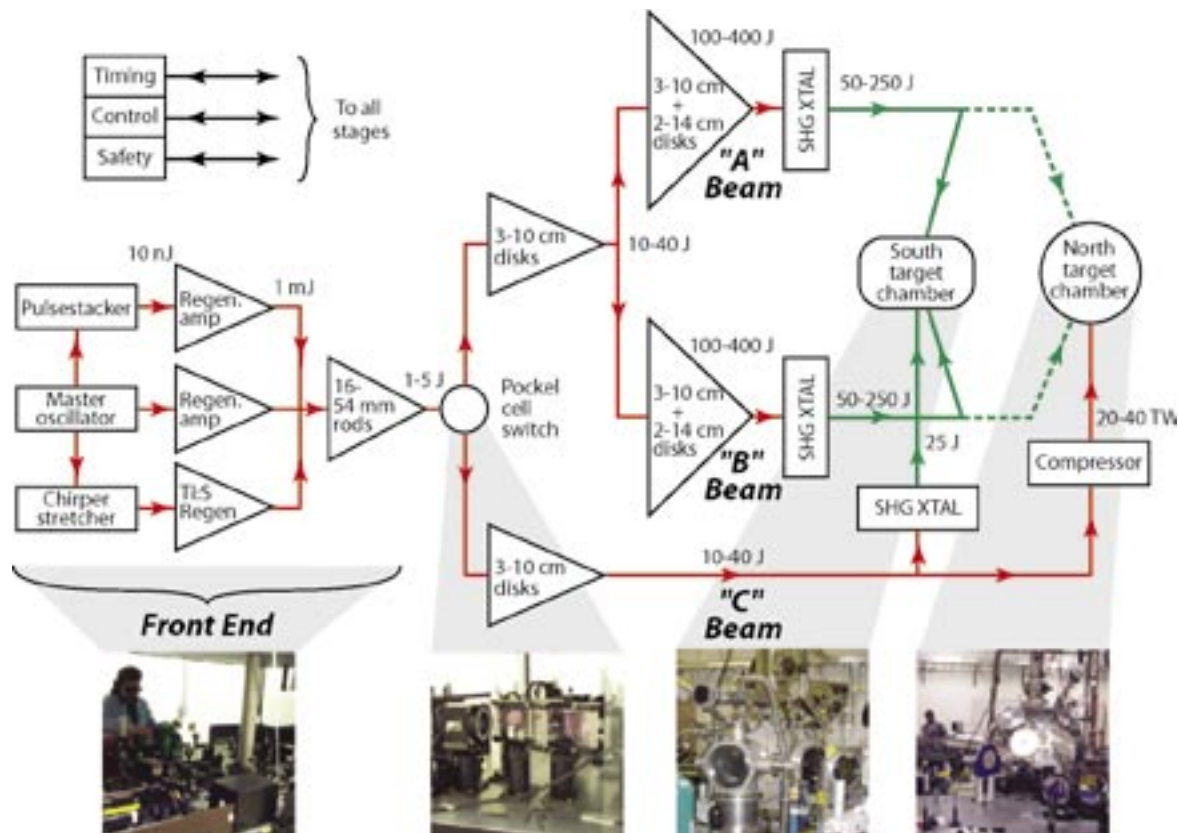
Trident's laser driver produces several hundred joules of energy over a pulse-length duration that spans more than 6 orders of magnitude from less than a picosecond to several microseconds. It uses an Nd:YLF master oscillator and three chains of Nd:glass rod and disk amplifiers in a conventional master-oscillator power-amplifier (MOPA) configuration (Figure 2) operating at 1,054-nm wavelength. Trident's main A and B beam lines, which use 14-cm-aperture amplifiers, produce the highest energy after frequency doubling and conversion into the 527-nm green light shown in Figure 1. The third C beam line, which uses 10-cm-aperture final amplifiers, produces lower energy but is more flexible with better beam quality, focus, and ability to be converted to other wavelengths. (Three beams—hence the name “Trident”!) The high-energy stages of the amplifier chain are shown in Figure 3. The laser-driver system operates in three different modes, depending on the pulse-

*Figure 1. View inside
Trident's target chamber.
Targets may be illuminated
with up to several hundred
joules of energy in pulses
ranging from picoseconds
to microseconds in length.*



Facilities Research Highlights

Figure 2. Trident's laser driver uses a conventional MOPA architecture. Main laser pulses (A and B beam lines) and auxiliary laser pulses (C beam line) are amplified sequentially through the front end of the laser system before they are routed to separate disk amplifier chains for further amplification. Shaping and timing can be controlled separately.



length range. For microsecond-length pulses, one regenerative amplifier is used as an oscillator and the frequency-doubling crystals are bypassed. For nanosecond-length pulses, output from the master oscillator is temporally shaped (Figure 4) before amplification. The C beam line pulse can be independently shaped and timed. It is also normally frequency-doubled to 527 nm but can also run at a fundamental output of 1,054 nm, at a third harmonic output of 351 nm, or at a fourth harmonic output of 263 nm. It can also be operated at reduced energy in a *single-hot-spot* (SHS) mode in which the spot on target is nearly diffraction-limited. For pulses in the picosecond range, the output of the master oscillator is frequency-broadened and “chirped” before amplification in the C beam line. The 1,054-nm output is then compressed with a pair of large diffraction gratings before being focused on target. Energies available on target are summarized in Table 1 and Figure 5.

Target Chambers

Experiments are regularly conducted in two high-vacuum target chambers, each in its own room. The south target chamber is a cylinder approximately

150 cm long and 75 cm in diameter (Figure 2). Single- or double-sided target illumination is possible through several 20-cm-diam ports on each end of the chamber. More than 40 smaller ports are available for diagnostic instrumentation. Individual targets are inserted through an airlock. The target insertion and positioning mechanism provides x-y-z and rotation adjustment under computer control with 1- μ m linear resolution and 350- μ rad angular resolution. The three-axis, target-viewing system has 20- μ m resolution. The chamber is fitted with a Nova-standard six-inch instrument manipulator (SIM) to accept all SIM-based instruments for checkout, characterization, or use.

Trident's north target chamber is a sphere with an inside diameter of 145 cm (Figure 2). This target chamber is capable of very flexible target illumination and diagnostic placement geometry because of the 92 ports, ranging in diameter from 2 in. to 14 in., distributed around the chamber surface. The target insertion and positioning mechanism is similar to that in the south chamber. The chamber is fitted with a standard ten-inch instrument manipulator (TIM) that accepts all TIM- and SIM-based instruments.

Trident Target Diagnostics

Optical diagnostics routinely used on Trident include illumination and backscattered-light calorimeters, backscattered-light spectrometers, and high-bandwidth (5 GHz) and streak-camera-based power monitors. Both point and line VISARs are also available. Filtered, photoconductive diamond detectors and x-ray streak cameras with < 10-ps resolution monitor the emission of x-rays from the target. A gated, filtered, x-ray imager provides 16 frames with 80-ps resolution. Various filtered x-ray power and spectral diagnostics covering 0 to 35 keV can be installed as needed. Static x-ray pinhole cameras are also available.

Table 2 summarizes the diagnostic instrumentation available on Trident. Most can be installed on either the north or south target chamber. Users are also welcome to provide their own unique instruments; interfacing information is provided upon request.

Administration

The Plasma Physics Group (P-24) operates Trident as a multipurpose facility for LANL and outside users (national laboratories, universities, and industry). Trident is funded largely through the Laboratory's Thermonuclear Experiments program element. The quality of proposed research and its

relevance to Laboratory missions are major criteria in determining what experiments are fielded on Trident. Proposals are normally solicited annually each winter for the following federal fiscal year.

Trident is located at LANL's Technical Area 35—an area open to visitors without security clearances. However, security plans are in place to permit appropriately cleared personnel to conduct classified experiments, if necessary.

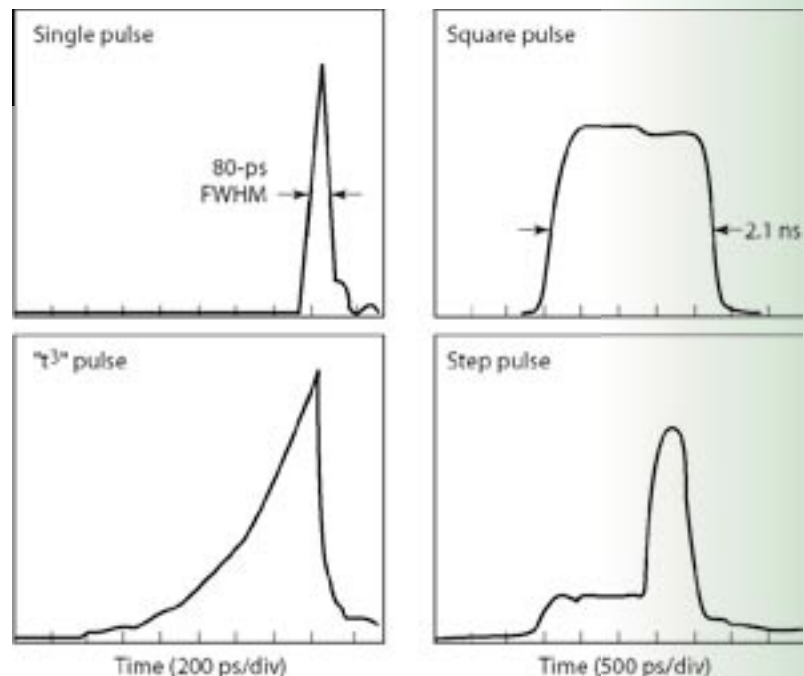
Acknowledgment

Many individuals beyond those presently operating Trident have contributed to its construction and operational success over the years, including Hank Alvestad, Tom Archuleta, Bentley Boggs, Max Byers, Paula Diepolder, Scott Evans, Jim Faulkner, George Faulkner, Jody Godard, Sam Letzring, Kent Moncur, Danielle Pacheco, Sam Reading, Tom Sedillo, Bob Watt, and scores of others. Trident is funded by the DOE Secondaries and Inertial Fusion Division.

Figure 3. Trident's two power amplifier chains feature 10- and 14-cm-aperture Nd:glass disk amplifiers (gray boxes) and a fully enclosed beam transport system (blue vacuum spatial filters and transport tubes).



Figure 4. Pulse-stacker output. These figures are examples of the diverse pulse shapes made possible by the coherent pulse stacker, which follows the master oscillator.



Facilities Research Highlights

Table 1. Trident target environment.

	A and B Beams		C Beam		
Parameters (units)	ns mode	μs mode	ns mode	SHS	ps mode
Wavelength (nm)	527	1053	1053/527 351	1053/527 351/263	1053
Pulse length (ns)	0.08–5.0	100–2000	0.1–2.0	0.1–2.0	0.7
Energy/beam (J)					
100 ps	50		50/30/20	5/3/1.5/0.5	30
1–2 ns	250		100/60/40		
100–2000 ns		300			
Spot diameter (μm)	100	100	50	5	20
Irradiance (W cm ⁻²)	10 ¹⁶		10 ¹⁶	10 ¹⁶	> 10 ¹⁹
Number of beams	2	1	1	1	1

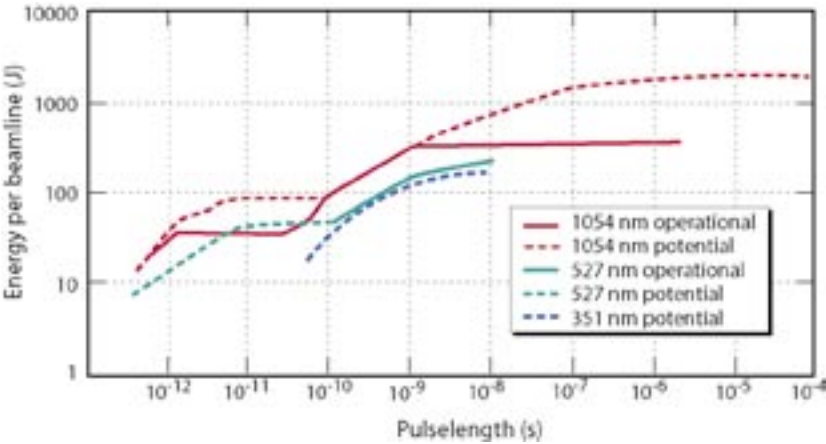


Figure 5. The laser driver operates over more than 6 orders of magnitude in pulse length. The solid lines show the energy that can presently be produced in one beam line. The dashed lines indicate energies that would be possible with modest enhancements. Red indicates 1,054 nm (infrared), green is 527 nm (green light), and blue is 351 nm (ultraviolet).

Table 2. Trident target diagnostics.

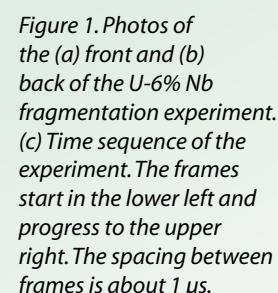
X-ray Diagnostics	Optical Diagnostics
Streak cameras	Streak cameras
CCD cameras	Spectrometers
Gated imagers	Backscatter diagnostics
Crystal spectrometers	Point and line-imaging interferometers (VISARs)
Grating spectrometers	CCD cameras
X-ray (and optical) photodiodes coupled to high-speed digitizers	
Microscope	

For more information about Trident, visit <http://plasmasys.lanl.gov/~knc/TRIDENT/tritecbl.htm> or contact Robert Gibson (505-667-5040, rbg@lanl.gov), Cris Barnes (505-665-5687, cbarnes@lanl.gov), or Allan Hauer (505-667-5167, hauer@lanl.gov).

When energetic charged particles travel through matter, the Coulomb force between the particles and the atomic nuclei in the medium leads to a large number of small deflections of the particle trajectories. The nature of the Coulomb interaction leads to a cross section for scattering that is not integrable, but, in aggregate, the multiple scattering of a particle can be treated analytically.¹ To a good approximation, the angular distribution that results when a particle of momentum p traverses from a length of material l is given by

$$\frac{dN}{d\Omega} = \frac{1}{2\pi\theta_0^2} e^{-\frac{\theta^2}{2\theta_0^2}}, \quad (1)$$
$$\theta_0 = \frac{14.1}{p\beta} \sqrt{\frac{I}{X_0}}. \quad (2)$$
$$X_0 = \frac{716}{Z(Z+1)\ln(287/\sqrt{Z})}. \quad (3)$$

Charged particles also scatter from electrons in the medium. Because the electrons are light, charged-particle scattering generally leads to continuous energy loss rather than to angular deflections. This energy-loss mechanism provides a method for detecting the particles. In proton and electron radiography, images can be formed on scintillator screens with high efficiency. For cosmic-ray muon radiography, the energy deposited in a multiwire drift detector is used to measure the trajectory of individual cosmic rays. Multiple scattering leads to a stochastic trajectory through the medium. This is one of the limitations of charged-particle radiography. Position resolution is ultimately limited by the scale established by the product, multiple-scattering angle, and object thickness, $\Delta x = k\theta_0 l$, where k is a case dependent constant of order unity.



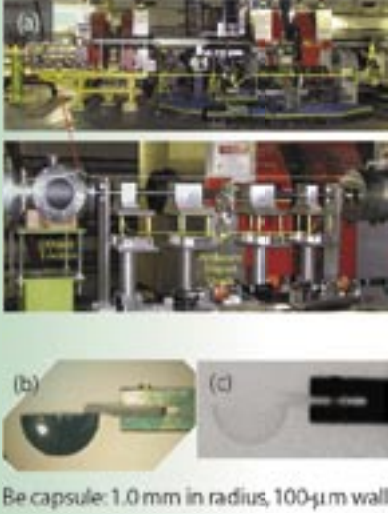


Figure 2. Photo of (a) the newly commissioned magnifier with images of one-half of a beryllium capsule (b) and its radiograph (c).

Radiography 2003

Proton radiography. Charged particles are bent by the Lorenz force in a magnetic field. Lenses that focus charged particle beams can be constructed from quadrupole magnets. Highly symmetric lens systems have been developed for pRad that sort the scattering angles in a beam transmitted by an object in one plane (the Fourier plane); these lenses then form an image of the transmitted beam in another plane (the image plane) further downstream.

Proton radiography was originally developed to take advantage of the enormous gain in statistical precision that can be obtained by using the long, hadronic mean-free path of protons, $\lambda_p = 200 \text{ gm/cm}^3$, when compared to the relatively short mean-free path of high-energy photons, $\lambda_\gamma = 25 \text{ gm/cm}^3$, for thick-object hydrotest radiography. This has been studied at the AGS at BNL using higher-energy proton beams (24 GeV/c) than those available at LANL (1.4 GeV/c), and indeed the expected advantage of about a factor of 100 over the first axis of DARHT has been demonstrated.²

The 800-MeV proton beam provided by the LANSCE accelerator has proven to be very useful for smaller-scale experiments, even though this energy is too low for hydrotest radiography, by using the principles laid out above. A collimator placed in the Fourier plane controls the contrast in the image plane by adjusting its size to provide the optimum contrast for a given experiment. The transmission through an object using a collimator that passes the transmitted beam up to some maximum angle, θ_c , can be calculated by integrating Equation 1:

$$t_{\text{tr}} = \int_0^{\theta_c} \frac{1}{\theta_0^2} e^{-\frac{\theta^2}{2\theta_0^2}} \sin(\theta) d\theta, \quad (4)$$

which for small angles gives

$$t_{\text{tr}} = (1 - e^{-\frac{\kappa}{l}}), \quad (5)$$

where

$$\kappa = \frac{\theta^2 p^2 \beta^2 X_0}{14 l^2} \quad (6)$$

Here, κ is the thickness scale set at the collimator angle cut. The collimator angle can be chosen to optimize the measurement of l for the most interesting part of an experiment for a given

incident number of particles, N_0 :

$$\frac{\Delta l}{l} = \frac{l}{\kappa} \frac{\sqrt{t_{\text{tr}}}}{1 - t_{\text{tr}}} \frac{1}{\sqrt{N_0}} \quad (7)$$

Equation 7 can be solved for a minimum as a function of κ . The result is $\kappa = 0.64 l$ (i.e., a transmission of 47%). From the discussion above, one sees that within the limits imposed by beam luminosity, pRad can be used for dynamic radiography on thin and thick systems. This is the observation that has made the pRad facility at LANSCE so useful to the weapons program.

Deuterium-uranium experiment. The fragmentation of shocked pieces of metal has been experimentally studied since the Civil War³ to obtain information needed for designing ordnance. Recently, models have been developed and incorporated into computer codes that may for the first time allow this phenomenon to be predicted.⁴ X-ray radiography can provide detailed snapshots of fragments in material at high strain rates in explosively driven experiments. The single images obtained cannot follow the time development of the material damage, and they are not quantitative. Although the x-ray experiments have been of great importance in the model development, pRad has been pursued because it can follow the time development of a single experiment (which is important because of the stochastic nature of these phenomena) and because it can provide quantitative data.

A recent series of experiments were performed on a strategically interesting material—uranium alloyed with 6% niobium. Small shells of this material were put under biaxial strain using a point-detonated hemispherical charge. A photo of one of these experiments along with a series of pRad images is shown in Figure 1. As can be seen, the fragmentation of the metal can be clearly followed.

Magnifier. Much the same as with an optical microscope, charged-particle images can be magnified using magnetic lenses. We have recently commissioned a proton magnifier (Figure 2) that uses permanent magnets to provide an enlarged image. Magnification also reduces the contribution of aberrations to the position resolution of the final image. As a consequence, the magnifier produced images with position resolution that is better than $15 \mu\text{m}$ over a 2-cm field of view, which is much better than the $200 \mu\text{m}$ that we have obtained with our larger lenses. This smaller field of view can be illuminated to a relatively high particle density with very short pulses from the LANSCE proton beam. We hope to perform studies of explosives and explosively driven phenomena on a much shorter length scale using this magnifier.

Charged-Particle Radiography—Providing New Methods of Imaging

Electron radiography. The NIF being built at LLNL has a goal of reaching thermonuclear ignition by driving the spherical implosion of a DT ice layer frozen to the inside of a capsule that is imploded using x-rays generated by very high-power laser beams. The time scale of the implosion is about 20 ns. The spatial and time scales and the dynamic range provide a challenge for existing diagnostics. The required position resolution of better than 10 μm can be obtained with charged-particle radiography using a magnifier. However, it would be difficult, as well as expensive, to obtain enough luminosity with a proton beam for this task.

We have performed studies of electron radiography to determine if it can cover the dynamic range of a NIF implosion. Because electron sources are very bright, we have shown that the intensity needed can be obtained from existing sources. Simulated radiographs at $t = 0$ and at $t = 17$ ns, nuclear time, for a NIF capsule are shown in Figure 3 for a simple permanent-magnet magnifier and a 400-MeV electron beam. These results indicate that the electrons may provide a unique diagnostic. Further theoretical studies are needed to ensure that the coupling between the electrons and the plasma do not perturb the image. Meanwhile, an electron accelerator and lens are being built at LANL to further study the experimental issues in electron radiography. The goal of this work is to provide a diagnostic tool for static radiography aimed at studying the uniformity of the ice layer inside of NIF capsules.

Muon radiography. An explosion, or even a fizzle, of a nuclear device in a major city would be catastrophic. The likelihood of such an attack from terrorist activities has been placed at 0.1–0.01 per year.⁵ The direct consequences in deaths and economic damage would dwarf the destruction of the World Trade Centers. The aftermath would be likely to shut down international trade. The impact on world economies would be enormous. Strategies to prevent nuclear weapons or the components needed to build them from becoming available to terrorists are currently being formulated. Components include tightly controlling the world's supply of fissile materials, reducing or diluting the material that is suitable for building nuclear weapons, and providing surveillance at transportation choke points to interdict the illicit transport of fissionable materials.

The essential component of any nuclear explosive device is the fissile core. This material is radioactive, emitting gamma rays, alpha particles, and neutrons. Both gamma radiation and neutron emission allow detection at a distance of meters. Detection schemes deployed to date have measured the gamma radiation or have used horizontal x-ray radiography

to try to image the material. The gamma radiation, however, is easily shielded with a few centimeters of lead, tungsten, or other heavy metal, and the radiography has been shown to be ineffective. X-ray radiography with currently deployed test systems has failed to detect shipments of depleted uranium.

We have investigated the feasibility of using cosmic-ray muon radiography for homeland defense and compared the process to other active radiography approaches. In muon radiography, the charged particles are cosmic-ray muons. Because of their low rates, the muons can be individually detected.

Conventional radiography takes advantage of the absorption of penetrating radiation. For x-ray radiography,⁶ the brightness of a pixel in the image is determined by the absorption or scattering of the incident beam:

$$N = N_0 e^{-\frac{L}{L_0}}, \quad (8)$$

where L is the path length (areal density) through an object, and L_0 is the mean-free path for scattering or absorption. The precision of radiographic measurements is limited by Poisson counting statistics of the transmitted flux,

$$\frac{\Delta L}{L_0} = \frac{1}{\sqrt{N}}. \quad (9)$$

The maximum mean-free path for photons in high-Z elements occurs at a few MeV. The mean-free path is approximately 25 gm/cm^2 for all materials at this energy. This corresponds to less than 2 cm of lead. To penetrate objects of tens of L_0 requires a large incident dose. An alternative is provided by charged-particle² radiography using cosmic-ray muons. In a 10-cm-thick layer, a 3-GeV muon (the average cosmic-ray energy) will scatter with a mean angle of 2.3 mrad in water ($X = 36$ cm), 11 mrad in iron ($X = 1.76$ cm), and 20 mrad in tungsten ($X = 0.56$ cm). If the muon-scattering angle in an object can be measured and if its momentum is known, then the path length, L , can be determined to a precision of

$$\frac{\Delta L}{L} = \sqrt{\frac{2}{N}}, \quad (10)$$

where N , the number of transmitted muons, is very nearly equal to the number of incident muons. Thus, each transmitted muon provides information about the thickness of the object.

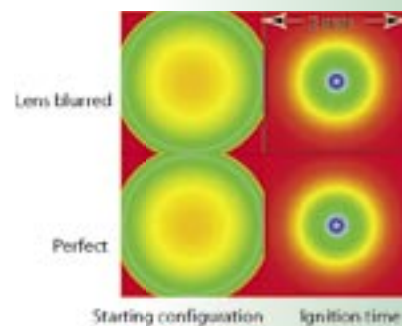


Figure 3. Simulated radiographs at $t = 0$ and $t = 17$ ns for a NIF capsule.

Facilities Research Highlights

We have constructed models of realistic shipping containers and vehicles for use in the Monte Carlo radiation codes known as MCNPX⁷ and GEANT.⁸ These have been used to compare existing x-ray and gamma-ray techniques with muon radiography. Muon radiography has been shown to discriminate all of the scenarios considered in less than four minutes scanning time. In Figure 4, a container has been filled with two layers of half-density iron balls, 20 cm in radius on 50-cm centers. A 20-kg sphere of high-enriched uranium has been hidden in the container. The muon radiograph in Figure 4 clearly shows the ease with which nuclear materials can be distinguished from background scatter. An x-ray radiography of a portion of the container, also shown in Figure 4, is plagued with problems from background scatter. Also, x-ray radiography does not provide three-dimensional views of a scene. Two-view x-ray radiography may be able to address some of these problems. The results of this study show that within the boundaries of weight limits, shielded containers of fissionable material can be easily obscured in ways that make it impossible to discriminate the material from legitimate cargo with x-rays. However, these are easily detected using muon radiography.

Conclusion

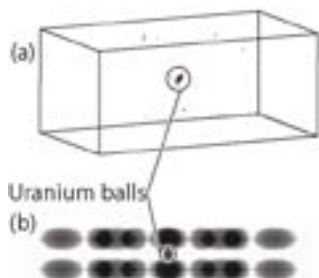
Charged-particle radiography is providing a versatile new probe that has advantages over conventional x-ray radiography for some unique applications. In pRad, charged-particle radiography has been used to make quantitative motion pictures of dynamic events. By taking advantage of magnetic lenses to magnify images and by using the very bright beams that can be made with electrons, we

have suggested that charged-particle radiography might even be useful for studying the fine spatial detail and very fast motion in a NIF implosion. Finally, we have demonstrated that radiographs can be made using cosmic-ray muons for homeland-defense applications.

References

1. B. Rossi, *High-Energy Particles* (Prentice-Hall, NJ, 1952), p. 66.
2. C.L. Morris *et al.*, "A comparison of proton and x-ray thick object radiography," *Defense Review*, to be published (2003).
3. G.T. Gray, private communication, 2003.
4. P.J. Maudlin, Weapons Working Group, Los Alamos National Laboratory, December 2003.
5. S.E. Koonin, "Concealed nuclear devices," Jason Fall Meeting, McClean, Virginia, 2003.
6. N.B. Konstantin, G.E. Hogan, C. Morris, W.C. Priedhorsky, A. Saunders, L.J. Schultz, and M.E. Teasdale, "Radiographic imaging with cosmic ray muons," *Nature* **422**, 277 (2003); W.C. Priedhorsky *et al.*, "Detection of high-Z objects using multiple scattering of cosmic ray muons," *Review of Scientific Instruments* **74**, 4294-4297 (2003); and L.J. Schultz, K.N. Borozdin, J.J. Gomez, G.E. Hogan, J.A. McGill, C. Morris, W.C. Priedhorsky, A. Saunders, and M.E. Teasdale, "Image reconstruction and material Z discrimination via cosmic ray muon radiography," *Nuclear Instruments and Methods in Physics Research*, in press (2003).
7. J.S. Hendricks *et al.*, "MCNPX, Version 2.5.c," Los Alamos National Laboratory report LA-UR-03-2202, (2002).
8. Application Software Group Computing and Networks Division, "GEANT detector description and simulation tool," CERN Program Library (W5013), <http://wwwasdoc.web.cern.ch/wwwasdoc/pdfdir/geant.pdf>.

Figure 4. (a) Muon-radiography result. The uranium is visible and easily detectable above a threshold automatically. (b) X-ray result. The contrast has been reduced by scatter background. The uranium is not easily detectable automatically and cannot be distinguished from the iron cargo automatically. It could be moved so that it is shielded by the iron.



For more information, contact Chris Morris at 505-667-5652, cmorris@lanl.gov.

Shock-Wave and Material-Properties Experiments Using the Atlas Pulsed-Power Machine

The Atlas facility built by LANL is the worlds first, and only, laboratory system designed specifically to provide pulsed-power-driven hydrodynamics capability for shock-wave physics, materials properties, instability, and hydrodynamics experiments in converging geometry. Constructed in 2000 and commissioned in August 2001, Atlas is a 24-MJ, high-performance capacitor bank capable of delivering up to 30 MA with a current rise time of 5–6 μ s. Atlas completed its first year of physics experiments in October 2002, using ultra-high-precision magnetically imploded, cylindrical liners to reliably and reproducibly convert electrical energy to hydrodynamic energy in targets whose volume is many cubic centimeters. Multiview (transverse and axial) radiography, laser-illuminated shadowgraphy, and VISAR measurements of liner and target surface motion, in addition to electrical diagnostics, provide a detailed description of the behavior of the experimental package. In the first year, material-damage and -failure experiments, dynamic-friction experiments, and a family of converging-shock experiments were conducted in addition to a detailed series of liner-implosion-characterization experiments. These experiments will continue, and an additional experimental series will be added in the future to evaluate material strength at very high rates of strain, ejecta formation from surfaces, and instability growth at interfaces.

*R.E. Reinovsky (P-DO),
C. Thompson (P-22),
W.L. Atchison, R.J. Faehl,
and I.R. Lindemuth
(X-1), R.K. Keinigs (X-4),
W. Anderson (MST-7), and
T. Taylor (MST-10)*

Ultra-high-precision cylindrical liners imploded with pulsed-power techniques have been applied to a variety of interesting questions broadly addressing the properties and behavior of condensed matter and plasmas. Generally, these topics fall into three categories:

- (1) the properties of condensed matter at the extremes of pressure, temperature, and energy density;
- (2) the hydrodynamic behavior of imploding systems; and
- (3) the properties and behavior of dense plasmas.

In the first category, pulsed-power-driven liner experiments can explore the EOS of materials and phase transitions under single-shock (Hugoniot) conditions at higher shock pressures than those attainable by two-stage gas-gun/flyer-plate techniques. Magnetic drive offers shockless compression^{1,2,3} that can drive materials to states not accessible through single-shock processes and to strains and strain rates far exceeding those available from other shockless techniques.

In the category of implosion hydrodynamics, liner-driven techniques are excellent for exploring

- instability growth in materials displaying full strength and in strengthless materials;
- the behavior of materials at interfaces (friction); and
- hydrodynamic flows in complex geometries.

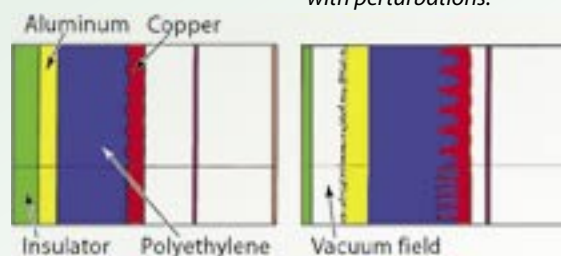


Figure 1. Multilayer liner with perturbations.

Facilities Research Highlights

In the third category, Atlas can produce plasmas in which the ion and electron physics are strongly coupled—where little experimental data are available. For the initial Atlas experiments, material strength and failure (spall), interfacial dynamics (friction), and complex hydrodynamic flow experiments were selected.

Material Properties

Pulsed-power-driven liners permit the study of strength of (and ultimately the failure of) materials under extremes of strain and the rate of strain. Because of cylindrical convergence, the inner surface of an imploding Atlas liner reaches strains exceeding 200% at strain rates of 10^4 to 10^6 per second. By proper choice of liner designs (e.g., a high-conductivity aluminum armature surrounding a thin cylinder of the material of interest), the test sample can be isolated from the effects of the drive (including magnetic fields and ohmic heating), and the acceleration can be applied in a way that ensures that the sample material is not shocked. A third layer, intermediate between liner and sample, can further isolate the sample from processes happening in the liner. This also allows additional control of the pressure history applied to the target. (Barns *et al.* pioneered such techniques with high explosives in 1974.⁴) For Atlas-based studies of material strength, a “three-layer liner” (Figure 1) has been designed by a joint LANL/VNIIEF team, including the All-Russia Scientific Research Institute of Experimental Physics (at Arzamas-16). The system employs an aluminum, current-carrying liner; a polyethylene intermediate layer; and a copper sample. Perturbations up to a hundred microns in amplitude and a few millimeters in wavelength are preformed (machined) into the outer surface of the copper sample. The perturbations can be detected by radiography before and during acceleration and are predicted to grow in amplitude by a factor of 2 to 8 during approximately 8 μ s of drive (Figure 2).

Figure 2. Perturbation growth for three-layer liners. A/A_0 is the amplitude ratio.

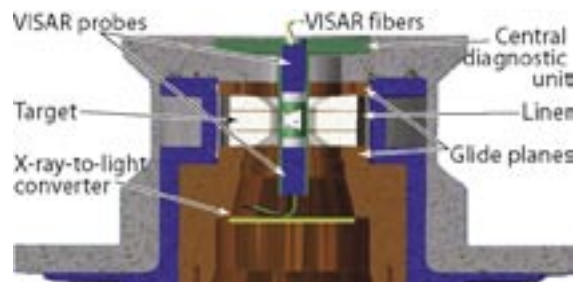
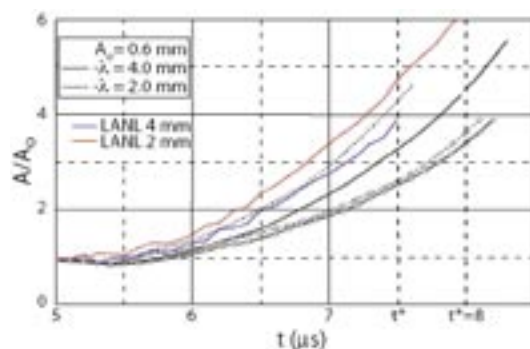


Figure 3. Atlas spall experiment.

While material-strength parameters can be deduced directly from the perturbation growth, the growth rates alone are sufficient to distinguish between several material models and among different computational techniques.

Liner implosions also offer unique opportunities for studying material failure (ultimate strength) at very high strain rates (in shocks) and at pressures that range from below the failure threshold to pressures many times that threshold. One convenient and familiar geometry for studying failure is the interacting shock geometry leading to “spall.” Implemented in cylindrical geometry, the experiment is described in Figure 3. A series of four Atlas experiments have been conducted using a specially characterized, grain-oriented aluminum target material (driven by an identical aluminum liner) at shock pressures of 40–110 kbar. With these parameters, the tension in the sample ranges from that producing incipient spall to parameters where the sample clearly fails. Material behavior is diagnosed by monitoring the (inner) free surface velocity using VISAR. Figure 4 shows VISAR measurements of inner-surface velocity at two points, including shock breakout; the “pull back” as material is placed in tension; and the ringing after material failure. From peak velocity and velocity at failure, a spall strength can be found using established analysis techniques. In addition to VISAR, both transverse and longitudinal radiography is used to image the formation of the spall layer. Postfailure metallurgy provides important information about the behavior of the material during a spallation event. The controllability of pulsed-power-driven liners allows recovery of both native material and, in some cases, even the spalled material for post-event analysis—this is a significant advantage.

Shock-Wave and Material-Properties Experiments Using the Atlas Pulsed-Power Machine

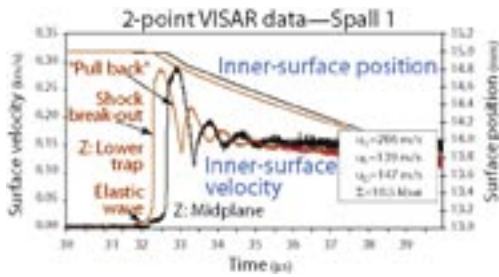


Figure 4. VISAR measurement of a spall experiment.

Implosion Hydrodynamics

Cartesian geometry is traditionally used to explore material properties; these studies of converging, liner-driven geometry represent an extension of those traditional methods. Symmetrical, radially imploding geometries can be readily studied by numerical simulation. Experimental data from configurations that are readily definable and calculable, but for which analytic solutions are not available, are important in benchmarking (both old and new) hydrodynamic (hydro) codes. The five-shot Atlas Hydro-Features (HF) series [preceded by the four-shot Near-Term Liner Experiments⁵ (NTLX) series] began the process of gathering such data and demonstrated a sophisticated suite of experimental diagnostics for liner-driven experiments. Both HF and NTLX series employed a high-precision, shocklessly accelerated aluminum liner that drove a symmetrical cylindrically converging shock in a tin shock receiver. Tin melts at relatively low shock pressure; in the HF and NTLX experiment series, the shocked tin is a strength-free liquid. The converging shock emerges from the tin into a lower-density, optically transparent medium (acrylic or water) where its motion is characterized by two diagnostics simultaneously (Figure 5). A two-pass, axially directed, laser-illuminated shadowgraph records the change in refractive index and opacity of the material during passage of the shock, and a multiframe axially directed x-ray radiograph (Figure 6) records the change in material density as the shock moves through the material. Because of radial convergence, the shock speed should increase slightly as the shock approaches the axis, and the shock should reflect from the axis and expand uniformly through the once-shocked medium. Simulating the reflected shock is nontrivial, and the Atlas data constitutes nearly the only experimental data with high enough fidelity and precision to challenge the computational codes.

The next most challenging configuration for the simulation tools is where the symmetrical shock in the receiver emerges asymmetrically into the inner medium. This is accomplished in the experiment by introducing an offset between the axis of the inner medium and the axis of the shock receiver. The shadowgraph and radiographic diagnostics show that the convergence of the shock in the inner medium arrives off-axis as predicted. Taken together, these data constitute a significant test of both old and new simulation tools.

The imploding liner also presents opportunities for exploring the differential motion of material at an interface. Typically, experimental data on the behavior of material at “sliding” interfaces are limited to modest relative velocities and modest normal pressures. As relative velocities between the materials increase, one model predicts (supported by molecular-dynamic simulation) that the material at the interface melts and the presence of liquid at the interface reduces the effective frictional force. An experiment (Figure 7) has been designed to explore parameter space where the interfacial velocity varies from just below that for which the frictional force peaks and extends to values three to five times that value. The first of these experiments was conducted on Pegasus in 1998 and the second on Atlas during this first year of operation. For these experiments, a very thick, slow-moving liner impacts a cylindrical target—providing a supported shock of several microseconds duration. The target was configured as a sandwich of circular disks with a low-density (aluminum) disk between two high-density (tantalum) disks. The converging shocks generated when the liner impacts the target produce different particle velocities in the aluminum and tantalum disks—resulting in relative motion at the interfaces while simultaneously

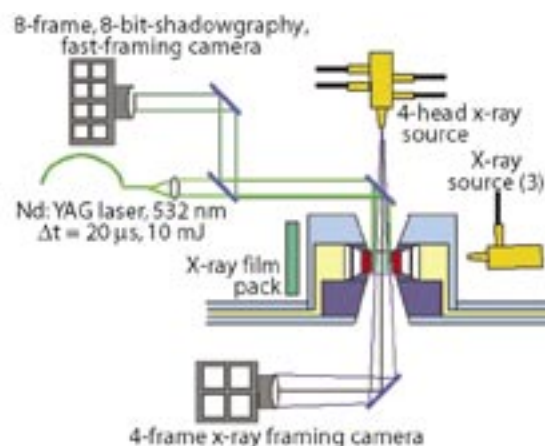
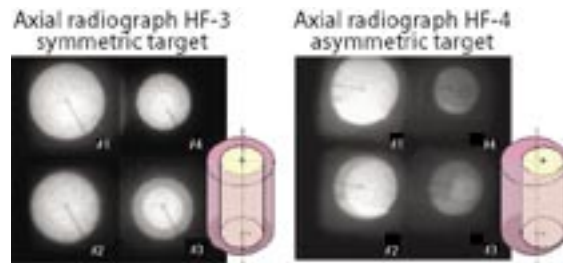


Figure 5. Diagnostics for HF experiments.

Material Studies Research Highlights

Figure 6. Radiographic data from symmetric and asymmetric targets. These are the third and fourth shots in the HF series.

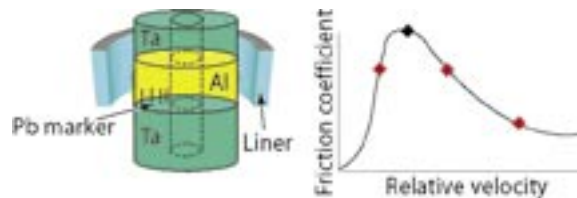


pressurizing the target. Lead marker wires, 200 to 300 μm in diameter, are imbedded in the aluminum and radiographed in the transverse direction. Development of the boundary-layer motion is diagnosed by radiographing curvature and distortion of the wires. The experiment is performed as a function of shock strength (relative interfacial velocity), materials, and surface condition.

Conclusion

The development of economical, highly reliable, low-impedance capacitor banks coupled to high-precision, near-solid-density liners imploding at 5 to 20 km/s have made possible a wide variety of hydrodynamic experiments. The uniformity, controllability, and high liner velocities enable experiments not otherwise possible and represent a complement to lasers and nanosecond pulsed power used for radiation-driven experiments.

Figure 7. Atlas friction experiment.



References

1. J.R. Asay, C.A. Hall, K.G. Holland *et al.*, "Isentropic compression experiments on the Z accelerator," in *Proceedings of the Conference of the American Physical Society Topical Group on Shock Compression of Condensed Matter*, M.D. Furnish, L.C. Chhabildas, R.S. Hixson (Eds.), (American Institute of Physics, 2000), Vol. 505 pp. 1151–1154.
2. D.G. Tasker, C.M. Fowler, J.H. Goforth *et al.*, "Isentropic compression experiments using high explosive pulsed power," in *Proceedings of the Ninth International Conference on Megagauss Magnetic Fields Generation and Related Topics*, V.D. Selemir and L.N. Plyashkevich (Eds.), (VNIIEF, Sarov, Russia, to be published 2004).
3. A.M. Buyko, G.G. Ivanova, I.V. Morozova *et al.*, "Computation of electrically exploded opening switch for capacitor bank Atlas," in *Proceedings of the Ninth International Conference on Megagauss Magnetic Fields Generation and Related Topics*, V.D. Selemir and L.N. Plyashkevich (Eds.), (VNIIEF, Sarov, Russia, to be published 2004).
4. J.F. Barnes, P.J. Blewett, R.G. McQueen *et al.*, "Taylor instability in solids," *Journal of Applied Physics* **45**(2), 727 (1974).
5. P.J. Turchi, K. Alvey, C. Adams *et al.*, "Design, fabrication, and operation of a high energy liner implosion experiment at 16 megamperes," *IEEE Transactions on Plasma Science* **30**(5), 1777–1788 (2002).

Acknowledgment

This work was supported by the NNSA Office of Defense Programs. The Atlas experimental team includes operational functions provided by P-22 and Bechtel Nevada; diagnostic functions provided by P-22 and MST-10; precision-fabrication functions provided by MST-7; and design, simulation, and analysis functions provided by X-1, X-2, and X-4.

For further information, contact Robert Reinovsky at 505-667-8214, bobr@lanl.gov.

Atlas is a Marx-based capacitor-bank driver designed to deliver currents up to 30 MA to cylindrical target assemblies for the purpose of conducting high energy-density, hydrodynamic experiments in convergent geometry. The experiments planned for the Atlas machine are predominantly metallurgical in nature and include, but are not limited to, studies in accelerated-membrane stability, spall, interfacial friction, and high-strain/high-strain-rate forms. The Atlas power-flow/experimental-fixture design allows highly uniform magnetic drive for this experiment type. Funding for the machine's construction at LANL was provided by a line-item congressional decision in 1999.

The bulk of the experimental-effort funding is seated in the stockpile stewardship program (from the Associate Director for Weapons Physics) with the inclusion of (by direction from the NNSA) basic science expected from academia and similar proposals. P, DX, MST, and X Divisions collaborated in Atlas experiments. The operations and diagnostics teams from Bechtel Nevada have also been involved in the design of experiment diagnostics and operations training to a very significant degree.

Atlas has proven to be a precise tool in the arena of hydrodynamics and can produce delivered energy within 1% repeatability. It was one of the first such capacitor-bank systems to be totally controlled and managed via fiber-linked (ethernet) programmable logic controllers. The Atlas machine was designed in semi-autonomous bank divisions called "maintenance units" that allow all of the safety (interlocks and readiness), charge, and fire sequences to be conducted and managed by computer control, thus allowing the machine's controllers to interface with and maintain awareness of many nodes of information and control.

Atlas construction was completed and the machine was commissioned in December 2000. A series of 16 program experiments were conducted through October 2002 at LANL before shutting down Atlas to move it to NTS. The disassembly and move to NTS began in fall 2002, wherein the machine was turned over to Bechtel Nevada. Atlas is presently being reassembled at a new facility in Area 6 at NTS by the Bechtel Nevada crew. This crew was trained on the machine at LANL while the first series of experiments was performed—both for proof of principle of the Atlas machine and to finalize the experience of operations for the Bechtel Nevada operations crew and experiment designers. Final reconstruction and recommissioning of Atlas at the NTS facility is planned for March 2004. Presently, 23 program experiments are planned for the first full year of machine operations at NTS. An April 2004 start date will mean that the first funded series (FY 2004) will cover about the first half of the 23 experiments.

Relocation of Atlas to the Nevada Test Site

R.E. Reinovsky (P-DO), J.M. Neff-Shampine, W.B. Hinckley, J.E. Martinez, M.C. Thompson (P-22)

Facilities Project Descriptions

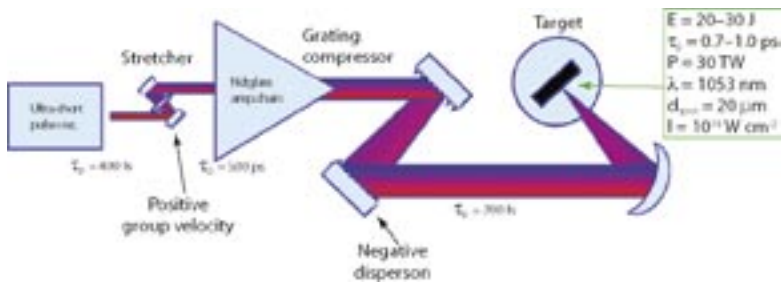
High-Energy Ultra-Short Laser Pulses at Trident

F.L. Archuleta, R.B. Gibson, R.P. Gonzales, T.R. Hurry,
R.P. Johnson, N.K. Okamoto, T.A. Ortiz, T. Shimada (P-24)

Extremely high peak power (10^{13} – 10^{15} W) lasers focused to spot sizes ~ 10 μm in diameter produce electric fields comparable to those found in intra-atomic regions, relativistic electron motion, and multimegagauss magnetic fields. These optical power levels open exciting opportunities for research in numerous areas such as intense x-ray sources, energetic-particle production, and the “fast-ignition” approach to ICF. Trident’s modest capability to produce high-peak-power, ultra-short (≤ 1 ps) pulses was replaced by a new system that produces 30 TW focused to an irradiance of $\sim 10^{19}$ W cm^{-2} in Trident’s north target chamber. The new capability makes use of most of the original pulse chirper and stretcher, the existing C-beam amplifier chain, and an entirely new large-aperture pulse compressor constructed next to the north target chamber where the amplified, chirped 0.5-ns pulse is temporally compressed about 1,000 times (with $> 75\%$ energy efficiency), which greatly increases its power (Figure 1). This compressor is built on a standard optical table rather than in the large vacuum vessel normally used. While the nonlinear susceptibility of air and the target-chamber vacuum window ultimately limit peak optical power, cost and time to implement the capability were an order of magnitude less than what a vacuum compressor of similar performance would have required. Because all Trident beams are derived from the same master oscillator, either of the main beam lines can be used simultaneously to preheat or compress a target with a nanosecond-duration pulse synchronized to the ultra-short pulse with negligible jitter.

Figure 1. High-energy, subpicosecond pulses are produced by chirping and stretching a low-level ultra-short pulse, amplifying it to a high level, and then compressing it. Large diffraction gratings are configured to be the temporally dispersive elements.

The ultra-short-pulse capability at Trident has now been used for approximately 100 target shots producing multi-MeV protons and ions and for the study of metal removal for the DoD. Other potential applications include pRad, intense x-ray generation, and the study of the fast-igniter approach to ICF.



Trident is LANL's multipurpose laboratory for conducting experiments requiring high-energy laser-light pulses. It supports laser-driven HED physics experiments and associated diagnostic development in ICF, weapons physics, and basic science. Trident has a three-beam frequency-doubled Nd:glass laser driver and two vacuum target chambers. It has operated reliably for a decade, principally at its design pulse-length range of 0.1–2.5 ns, producing up to 250 J in each of its two main beam lines and up to 60 J in the third, smaller beam line. In FY 2002 and FY 2003, a high-energy ultrashort-pulse capability was added, producing 20–30 TW in a subpicosecond pulse. Production of multi-microsecond infrared pulses also became more routine. This flexible facility now conducts experiments over more than 6 orders of magnitude in pulse length.

More than 800 high-energy target shots are fired in approximately 20 experimental campaigns each year. In FY 2002 and FY 2003, Trident

- hosted laser-plasma-interaction experiments that verified nonlinear dispersion relations;
- developed 1.5-keV large scale-length plasmas;
- developed and characterized moderately collisional, moderately coupled plasmas;
- studied the transition from fluid to kinetic nonlinearity for Langmuir waves; and
- studied stimulated-Brillouin-scattering detuning by a velocity gradient.

Laser-induced MeV proton beams were produced, characterized, and used for radiography. Laser-launched flyer plates were launched into several different materials to study EOS and other properties. In addition, high-speed imaging cameras are routinely checked out, debugged, and calibrated at Trident before being used at other laboratories.

Trident Laboratory Operations

*F.L. Archuleta, R.B. Gibson, R.P. Gonzales, T.R. Hurry,
R.P. Johnson, N.K. Okamoto, T.A. Ortiz, T. Shimada (P-24)*